On heavy particle-wall interaction in axisymmetric plasma discharges

A. Domínguez-Vázquez, F. Cichocki, M. Merino, P. Fajardo, E. Ahedo
Universidad Carlos III de Madrid, 28911 Leganés, Spain
July 19, 2021

Abstract

The effects of heavy particle-wall interaction on a cylindrical plasma source discharge are investigated, through hybrid particle-in-cell/fluid simulations. The bulk plasma is considered quasineutral with isothermal electrons, and with no secondary electron emission from the walls. The neutral gas wall reflection model is shown to play a major role in determining the conditions for a self-sustained and stationary plasma discharge. A hysteresis cycle on the injection mass flow rate is found when neutrals deviate from a purely diffuse reflection at the walls, with the mass utilization efficiency changing up to 20% between purely specular and diffuse scenarios. However, as the ratio of ionization mean free path to macroscopic length is decreased, the neutral-wall reflection model becomes irrelevant. Finally, even small deviations from unity of the ion energy accommodation coefficient at the walls are seen to have a major impact on both the ion and neutral distribution functions, and ultimately the mass utilization efficiency. This behavior stresses out the importance of a precise experimental determination of this parameter for accurate simulations.

1 Introduction

The plasma-wall interaction is a relevant research topic for the low-pressure plasma sources community, including plasma propulsion, due to the high surface-to-volume ratio of the considered devices. In fact, it greatly affects both performance and lifetime of plasma thrusters, since it is responsible for power losses, ion recombination and chamber walls erosion [1–3], and determines the plasma properties achieved inside low-pressure plasma sources to a high degree [4].

Since the involved physics and timescales are very different depending on the considered impacting particle, it is natural to analyze separately the wall interaction of electrons and heavy particles (ions and neutrals). Regarding the former, the electron fluxes to the walls and the secondary electron emission (SEE) are the main responsible, in typical low-collisional regimes, for the deviation of the electron velocity distribution function from a Maxwellian, and significantly affect the source performance. In this respect, a great effort has been put into exploring such effects, and a large number of plasma thrusters simulation codes including detailed sheath models accounting for SEE and partial thermalization of the electron population have been developed [2, 5, 6].

Regarding the heavy particles, their interaction with a wall is a complex process, whose collision outcome depends on a large number of factors, such as the impacting particle and wall atoms species, the impact energy and angle and the surface properties such as its roughness, chemical composition, cleanliness and temperature. Given this vast set of dependencies, most simulation codes use simplified phenomenological interaction models [7–9] featuring unknown parameters that are set *ad-hoc* to reproduce approximately the expected physics. In some particular scenarios, these unknown parameters can be inferred or directly obtained from experiments, such as in-orbit measurements of the drag coefficient [8,10], or from complex solid matter computer simulations which model the interaction of the impacting particle with the atoms of the surface material lattice [11]. However, in the context of plasma thrusters and sources, very few sensitivity analyses have been carried out to address their effects [4, 12, 13]. The heavy particle-wall interaction, especially regarding neutrals, has been studied more in depth in fusion devices [14, 15] than in plasma sources, in spite of an ionization degree which is much larger in the former (e.g. 99% vs 10%). Interestingly, these studies have shown that the neutral-wall interaction physics still plays a major role there, at least in determining the neutrals density distribution inside the reactor.

This paper focuses on the study of the effects of the heavy particle-wall interaction on a cylindrical plasma source, using a 2D axisymmetric quasineutral particle-in-cell (PIC) code with a simplified isothermal electron population, modeled through a Boltzmann relation [16]. This permits us to focus primarily on the heavy particle-wall interaction physics, without worrying about the coupling with an energy balance equation for the electrons. The effects of the neutral-wall reflection and ion recombination physics are analyzed separately. Regarding the former, it directly affects the plasma discharge ignition process: all plasma sources are in fact ignited by providing at the same time both a minimum neutral mass flow and an appropriate power, that can be given as an electric voltage between electrodes or as an input electro-magnetic wave, both producing an avalanche of free electrons and a sustained ionization regime. Being the neutrals the dominant population at ignition, their interaction with the walls plays a major role in the ignition physics, especially for plasma sources with such a high surface-to-volume ratio. While the assumptions of quasineutral plasma and Boltzmann electrons of

the considered PIC model do not permit to properly simulate the very early transient stages of the discharge, characterized by electron ionization avalanches and non-neutrality, in this work we focus on assessing the neutral properties required for a self-sustained stationary discharge, including the injection mass flow.

The two main figures of merit characterizing the neutral interaction with a material surface are the angular distribution and the energy of the reflected neutrals. These depend on the degree of accommodation of neutral particles with the material: the higher this degree, the more closely the reflected particle energy adjusts to the thermal energy of the surface. Some experiments indicate that the gas diffuse reflection with complete thermal accommodation represents satisfactorily the real gas-wall interaction process in most practical scenarios [7]. However, it is known that some factors such as the relative size of the gas and wall molecules, the surface roughness and contamination, due for example to gas-surface adsorption, and the gas molecules impact angle and translational energy relative to the surface can have non-negligible effects. In this respect, surface contamination generally increases the energy accommodation and broadens the angular distribution of the reflected population, thus approaching a diffuse reflection behavior [8,17,18]. In the context of numerical simulation codes, a common practice is to use the Maxwell model [9], which assumes complementary probabilities for specular and diffuse reflections with a given accommodation coefficient (generally used only for the diffuse reflection outcome). Other existing models, like Schamberg model [8, 9], take into account a combination of diffuse reflection and quasi-specular reflection (within a quasi-specular reflection cone) which are dependent on the incident angle. In this paper, both Maxwell limit cases (specular and diffuse) and Schamberg model are considered to evaluate their effects on the conditions required for a self-sustained and stationary plasma discharge and the plasma discharge characteristics.

In what regards the ions-wall interaction, before colliding with the walls and recombining with a wall electron, ions typically cross a Debye sheath that separates the plasma bulk from the wall. In most plasma sources, these walls are dielectric, so that the wall tends to be at a floating potential with respect to the plasma. This means that the potential drop through the sheath is several times the local electron temperature and is generally larger than the total kinetic energy acquired by the ions across the bulk plasma. This holds true in most of the plasma source chamber, with the exception of those regions characterized by either an intense ion axial acceleration or by a strong secondary electron emission, which can reduce importantly the potential drop through the sheath. In these regions, more grazing ion incidences can be expected, as confirmed by previous studies performed for a Hall effect thruster (HET) [19, 20]. On average, however, and with the above mentioned exceptions, very few ions hit the walls with grazing incidence, and the average impact angle does not deviate much from the normal incidence. Therefore, the recombination neutrals are generally re-emitted along a direction that follows a Lambertian (i.e. cosine) emission law. Regarding the re-emission energy, on the other hand, little experimental data is available and the existing one generally refers to accommodation of high energy neutrals during atmospheric re-entry [8, 10] and not to the ion energy accommodation with the interior walls of an electric thruster, where intrusive diagnostics are seldom found. Gibson, in Ref. [4], analyzes the effects of the wall accommodation coefficient with the walls of different oxygen species (including molecular and atomic oxygen ions) in a low-pressure discharge and considers a large range [0.1-0.95] in the absence of available direct measurements. In this work, we shall explore different values of the accommodation coefficient between 1 (perfect wall accommodation) and 0.9, which is consistent with recent experimental measurements for Xe ions impacting on a metallic surface with an energy of around 100 eV [21]. Moreover, both the ion and neutral distribution functions at the wall are analyzed for the mentioned wall accommodation coefficients, and their relation with the neutral reflection model described above are also investigated.

The rest of the paper is as follows. The considered plasma discharge model is presented in Sec. 2.1, while Sec. 2.2 focuses on the particle-wall interaction modeling. The simulation setup is described in Sec. 3.1, together with the nominal case results. The effects of the neutral-wall reflection physics on the plasma discharge are analyzed in Sec. 3.2, while the ion-wall interaction effects are discussed in Sec. 3.3. Conclusions are presented in Sec. 4, while two appendices describe numerical discharge triggering approaches and mesh convergence analysis.

2 Models

2.1 PIC model of the discharge

A detailed description of the PIC model used for the heavy species can be found in Refs. [16] and [22], and it is only briefly outlined here. The PIC model advances heavy species macroparticles in time and performs operations such as injecting them from dedicated boundaries, moving them according to Newton equation and the local electric field $\boldsymbol{E}$, computing collisions (e.g. ionization or charge-exchange reactions), simulating their interaction with material walls (further detailed in Sec. 2.2), and finally weighting them to the mesh nodes to obtain plasma and neutral gas bulk properties such as the number density and the particle fluxes/currents. These weighted plasma/neutral gas properties are used by the collisional algorithms, as detailed below, and to

update the electric potential according to an isothermal Boltzmann relation. The corresponding electric field is then used by the PIC model to advance the macroparticles in the next time step.

The presented model assumes quasineutrality, so that the plasma density n_e equals the ion density n_i where only singly-charged ions are considered. By neglecting the effects (minor) of electron collisions, the electric potential ϕ can then be obtained with the well known Boltzmann relation:

$$\phi = \frac{T_\mathrm{e}}{e} \log\left(\frac{n_\mathrm{e}}{n_\mathrm{e0}}\right), \tag{1}$$

where T_e is the constant electron temperature in energy units and n_e0 is a reference plasma density at the location where $\phi = 0$.

Regarding the ionization collisions, the approach implemented is based on the method developed for HPHall [23]. We describe here the general approach for the case of the single ionization reaction $A + e \rightarrow A^+ + 2e$, which is the only one considered in the present study. First, a deterministic sampling of the existing neutral macroparticles in a given mesh cell is performed, so that all of them have their weight reduced due to ionization. Then, the mass of new singly-charged ions Δm_i to be generated in the cell of physical volume V_c during the timestep Δt is

$$\Delta m_\mathrm{i} = m n_\mathrm{e} n_\mathrm{n} R_{01}(T_\mathrm{e}) V_\mathrm{c} \Delta t, \tag{2}$$

where m is the gas atom mass, n_e and n_n are the plasma and neutral densities, respectively, and $R_{01}(T_\mathrm{e})$ is the ionization rate, evaluated at the (constant) electron temperature T_e. Xenon gas is considered in the present study, with $R_{01}(T_\mathrm{e})$ following the Drawin model [24].

The number of new ion macroparticles to be generated in the cell is then obtained through a dedicated population control algorithm detailed in Ref. [16]. The new ion macroparticles are uniformly distributed within the cell, with their velocities sampled from a Maxwellian distribution with the corresponding neutral mean velocity and temperature. Finally, every neutral in the cell suffers a macroparticle weight reduction proportional to its weight, so that the total neutral mass loss in the cell equals the generated ion mass Δm_i.

2.2 Wall-particles interaction models

The Maxwell model assumes that the outcome of a particle-wall interaction can be either a perfectly specular reflection with probability p_spec or a purely diffuse reflection with probability $1 - p_\mathrm{spec}$. In the purely diffuse reflection case, sketched in Fig. 1(a), the reflection direction follows a cosine law, meaning that the probability of reflecting the particle within a solid angle $\mathrm{d}\Omega = \sin\theta \mathrm{d}\theta \mathrm{d}\lambda$ is $f(\Omega)\mathrm{d}\Omega = \cos\theta \mathrm{d}\Omega$, where θ is the angle between the surface normal and the reflection direction, and λ defines the reflection direction in the impact plane (polar angle between a reference plane direction and the projection of the reflected velocity). Recall that:

$$\int_\Omega f(\Omega)\mathrm{d}\Omega = \int_0^{2\pi} \mathrm{d}\lambda \int_0^{\pi/2} f(\theta,\lambda)\sin\theta \mathrm{d}\theta = 1 \tag{3}$$

In the specular reflection case, shown in Fig. 1 (b), on the other hand, the reflection angle θ is always equal to the impact angle θ_imp, while the projections of the reflection and impact velocities on the impact plane are aligned: $\lambda = \lambda_\mathrm{imp}$.

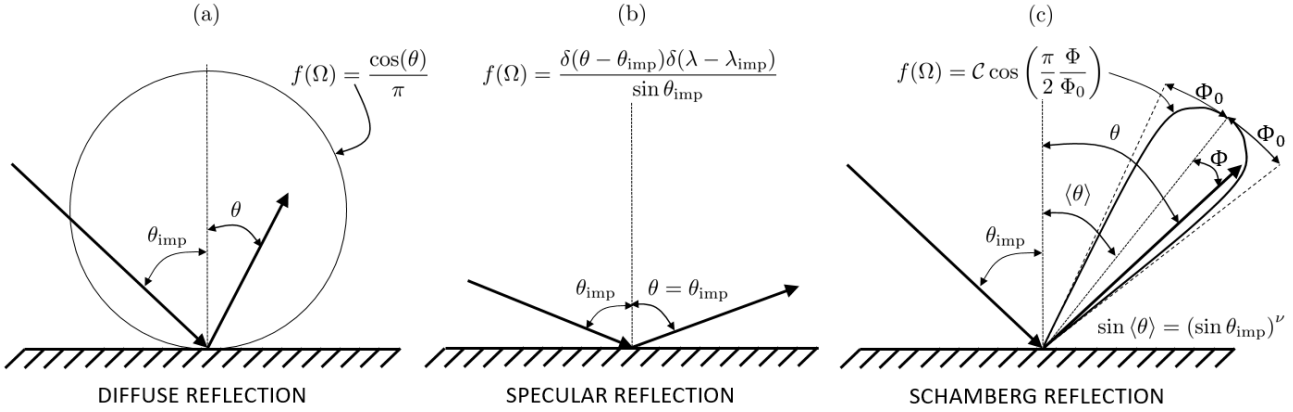

Figure 1: Schematics of the reflection for (a) Maxwell diffuse reflection, (b) Maxwell specular reflection, and (c) Schamberg reflection models.

The Schamberg model [8,25] is illustrated in Fig. 1 (c). First of all, the mean reflection angle $\langle\theta\rangle$ is obtained as:

$$\sin\langle\theta\rangle = (\sin\theta_{\mathrm{imp}})^{\nu}\,, \tag{4}$$

where ν is a parameter to be tuned. As for the specular reflection, the polar angle (in the impact plane) of the mean reflection direction is $\lambda = \lambda_{\mathrm{imp}}$. The stochastic reflection direction then belongs to a 3D cone featuring the mean reflection direction as symmetry axis and a semi-aperture $\Phi_0 \leq \pi/2 - \langle\theta\rangle$ (to avoid reflections into the surface). The probability of reflecting the particle at an angle Φ with respect to the mean reflection direction $\langle\theta\rangle$ then follows a cosine law:

$$\begin{cases} f(\Omega) = \mathcal{C}\cos\left(\dfrac{\pi}{2}\dfrac{\Phi}{\Phi_0}\right) & \text{if} \quad \Phi \leq \Phi_0, \\ f(\Omega) = 0 & \text{if} \quad \Phi > \Phi_0, \end{cases} \tag{5}$$

where the constant can be obtained by satisfying Eq. (3), which yields [25]:

$$\mathcal{C} = \frac{1}{2\pi}\frac{1-[\pi/(2\Phi_0)]^2}{1-[\pi/(2\Phi_0)]\sin\Phi_0}. \tag{6}$$

The Schamberg model tends to reproduce the Maxwell specular reflection if $\nu = 1$ and $\Phi_0 = 0$, and the Maxwell purely diffuse reflection if $\nu \to \infty$ and $\Phi_0 = \pi/2$ (and the constant $C \to 1/\pi$). However, as pointed out by Moore [25] for what concerns the calculation of the drag coefficient of a LEO satellite, the extreme specular/diffuse cases do not necessarily define the interval in which intermediate reflection types fall. For this reason, in Sec. 3.2, we shall compare the purely specular/diffuse reflection cases to an intermediate Schamberg model featuring $\nu = 2$ and $\Phi_0 = \pi/2 - \langle\theta\rangle$. This choice of the model is particularly meaningful as it permits to reproduce a quasi-diffuse reflection when the impact angle is $\theta_{\mathrm{imp}} \approx 0$ and a quasi-specular reflection with shrinking cone semi-aperture when $\theta_{\mathrm{imp}}, \langle\theta\rangle \to \pi/2$ (in fact $\Phi_0 \to 0$). This dependence of the reflection direction on the impact angle has been observed in many experimental characterizations and numerical simulations, such as those of Ref. [11] showing, for impact energies below 2 eV (and wall temperatures up to 300 K), a quasi-specular reflection for grazing incidence particles, and much more diffuse reflection patterns for particles impacting along the normal direction (a behavior which extends to higher θ_{imp} when the surface temperature increases).

The stochastic character of the reflection direction is physically related to the energy accommodation process that an impacting particle undergoes with the material surface [8,9,25]. The more complete the energy accommodation process, the closer the reflection direction to the diffuse pattern. Introducing a wall accommodation coefficient $\alpha_{\mathrm{W}} \in [0,1]$, the mean energy of the re-emitted/reflected particle is given by:

$$\langle E\rangle = (1-\alpha_{\mathrm{W,s}})\langle E_{\mathrm{imp}}\rangle + \alpha_{\mathrm{W,s}}E_{\mathrm{W}}, \tag{7}$$

where the index s refers to the impacting particle population ($s = \mathrm{i,n}$ for respectively ions and neutrals), $\langle E_{\mathrm{imp}}\rangle$ is the average incident particle energy and E_{W} is the average emission energy of a particle population in thermal equilibrium with the material surface. For a semi-Maxwellian thermal emission, this average wall energy is directly related to the material surface temperature T_{W} (in energy units) by $E_{\mathrm{W}} = 2T_{\mathrm{W}}$.

The energy accommodation coefficient generally depends on many factors, such as the relative size of the gas and wall atoms/molecules, the surface cleanliness and roughness, and both the impacting particle energy and direction. A clean and low-roughness surface will generally feature a larger probability of quasi-specular reflection with lower accommodation coefficients. In general, the wall accommodation process is more complete (and hence $\alpha_{\mathrm{W,s}}$ is higher), the lower the impacting particle energy, since less collisions with the surface atoms are needed for thermalization (in a single particle-wall interaction event) [8], and the lower the impact angle θ_{imp}, as this affects the particle-surface interaction time (which is maximum/minimum at respectively normal/grazing incidences). The latter dependence has been observed in measurements of neutral particles reflection off the surface of a spacecraft in Low Earth Orbit [10], characterized by a relatively high fraction of purely diffused particles (97%), due to their nearly normal incidence (thermal atom velocities are negligible with respect to the orbital velocity).

In the context of low-pressure plasma discharges, neutrals are generally a low energy population, with a kinetic energy of fractions of eV. At these energy levels, most neutrals will therefore be reflected diffusely with a high energy accommodation, taking also into account that the walls roughness increases during the operational lifetime of the device, due to ion sputtering and contamination. Nevertheless, a purely diffuse reflection model tends to overestimate the residence time in the chamber for those neutrals that hit the walls at grazing incidence, and this can have a non-negligible effect on the discharge, as we shall see in Sec. 3.2. In this context, the proposed Schamberg model, with $\nu = 2$ and $\Phi_0 = \pi/2 - \langle\theta\rangle$, should provide more realistic results.

Since the reflection direction and the energy accommodation coefficient are ultimately related, also the latter should depend somehow on the impact angle. In the absence of available experimental data to characterize the functional dependence $\alpha_{\mathrm{W,n}}(\theta_{\mathrm{imp}})$, in this work, we simplify the analysis and focus only on the effects of the neutral reflection direction. Therefore, and also for a fair comparison with the specular reflection case (characterized by a perfect energy conservation), a zero energy accommodation coefficient (i.e. $\alpha_{\mathrm{W,n}} = 0$) is considered for neutrals-wall reflection. This is not a strong assumption if the injected neutrals are close to thermal equilibrium with the discharge chamber walls, which is reasonable to assume.

Regarding the ions-wall interaction, a different model is considered due to two main reasons. First of all, ions accelerate through a plasma sheath before impacting the walls, so that their impact angle θ_{imp} is typically quite small (nearly normal incidence), as we will see in Sec. 3.3. Secondly, ions hitting the walls lose their kinetic energy very quickly and recombine with wall electrons. Therefore, we have assumed that ions recombine completely into neutrals and these are re-injected into the domain with a wall accommodation $\alpha_{\mathrm{W,i}} \in [0.9, 1]$, and following a purely diffuse reflection pattern. In the present quasineutral model, the simulation domain extends up to the sheath edge, and the thin plasma sheaths that develop around the walls are treated as surface discontinuities and solved separately. In particular, the potential fall in the sheath is taken into account in the computation of the ion wall-impact energy and angle. Under the assumptions of a planar, unmagnetized and collisionless sheath, the zero net current collected at the dielectric walls implies that this potential drop is given by

$$\Delta\phi_{\mathrm{sh}} = \frac{T_{\mathrm{e}}}{e} \ln\left(\frac{1}{M_{\mathrm{ri}}}\sqrt{\frac{m_{\mathrm{i}}}{2\pi m_{\mathrm{e}}}}\right), \tag{8}$$

where $M_{\mathrm{ri}} = u_{\mathrm{ri}}/c_{\mathrm{s}}$ is the ion fluid Mach number along the radial direction at the sheath edge (i.e. perpendicular to the walls) with $c_{\mathrm{s}} = \sqrt{T_{\mathrm{e}}/m_{\mathrm{i}}}$ the (constant) cold-ion sound speed based on the (constant) electron temperature, and m_{e} and m_{i} are the electron and ion elementary masses, respectively.

In the most general case of non-monoenergetic ions, a stable and monotonically decreasing potential solution of the Poisson equation within a thin collisionless unmagnetized sheath requires the fulfillement of the kinetic Bohm Criterion (BC) [26]. As detailed in Ref. [27], this implies that, at the sheath edge of the dielectric lateral walls,

$$M_{\mathrm{k}}^2 = \frac{n_{\mathrm{e}}}{T_{\mathrm{e}} P_2} \geq 1, \qquad P_2 = \int_0^\infty dv_{\mathrm{ri}} \frac{F(v_{\mathrm{ri}})}{m_{\mathrm{i}} v_{\mathrm{ri}}^2}, \tag{9}$$

where M_{k} is the so called Mach-Bohm number, v_{ri} is the ion radial particle velocity (i.e. perpendicular to the lateral dielectric walls), and $F(v_{\mathrm{ri}})$ is the one-dimensional normal velocity ion distribution function at the sheath edge (recall that only singly-charged ions are considered in this study). For non-monoenergetic ions, $M_{\mathrm{k}}/M_{\mathrm{ri}} < 1$ due to the dominant contribution of slow ion particles in the moment P_2 of Eq. (9). In the present code, if ions hitting material walls do not satisfy the kinetic BC, a plasma density correction is applied to produce a larger normal electric field that accelerates them to sonic conditions [27]. As a consequence, in the general scenario with non-monoenergetic ions, the fulfillment of the kinetic BC yields $M_{\mathrm{ri}} > M_{\mathrm{k}} \geq 1$.

Finally, the three-dimensional distribution functions of the impacting neutrals and ions $F'(E_{\mathrm{imp}}, \theta_{\mathrm{imp}}, \lambda_{\mathrm{imp}})$, depending on the impacting energy E_{imp}, impacting angle θ_{imp} and in-plane direction λ_{imp}, are integrated twice to yield the one-dimensional energy distribution function, $F(E_{\mathrm{imp}})$, and impact angle distribution function, $F(\theta_{\mathrm{imp}})$, defined as

$$F(E_{\mathrm{imp}}) = \int_0^{\pi/2} \mathrm{d}\theta_{\mathrm{imp}} \int_0^{2\pi} F'(E_{\mathrm{imp}}, \theta_{\mathrm{imp}}, \lambda_{\mathrm{imp}}) \mathrm{d}\lambda_{\mathrm{imp}}, \tag{10}$$

$$F(\theta_{\mathrm{imp}}) = \int_0^{\infty} \mathrm{d}E_{\mathrm{imp}} \int_0^{2\pi} F'(E_{\mathrm{imp}}, \theta_{\mathrm{imp}}, \lambda_{\mathrm{imp}}) \mathrm{d}\lambda_{\mathrm{imp}}, \tag{11}$$

with

$$\int_0^\infty F(E_{\mathrm{imp}}) \mathrm{d}E_{\mathrm{imp}} = \int_0^{\pi/2} F(\theta_{\mathrm{imp}}) \mathrm{d}\theta_{\mathrm{imp}} = -\boldsymbol{g}_{\mathrm{imp}} \cdot \boldsymbol{n}. \tag{12}$$

In the above equation, $\boldsymbol{g}_{\mathrm{imp}}$ and $\boldsymbol{n}$ represent respectively the impacting particle flux vector (not including reflected particles) and the normal unit vector at the wall, pointing towards the plasma. In a PIC model like the one considered in this work, these distribution functions are obtained by sorting impacting particles from any direction in the impact plane with any energy, in terms of the impact angle $F(\theta_{\mathrm{imp}})$, or from any direction in the impact plane and any impact angle, in terms of the impact energy $F(E_{\mathrm{imp}})$.

3 Simulation results

3.1 Simulation setup and nominal case results

The simulation domain considered corresponds to a cylindrical channel of 1 cm radius and 3 cm length, typical of HPT or ECR thrusters, presenting a surface-to-volume ratio of 200 m^{-1} (where only the lateral material wall has been taken into account). Fig. 2 shows the PIC mesh, which is structured and non-uniform in both directions, with an exponential law distribution. The spacing is minimum close to the injection boundary (green) and the lateral walls of the cylinder (red), where the largest plasma gradients are expected. The convergence analysis that has led to this PIC mesh is reported in Appendix A, while the mesh properties and the main simulation parameters are listed in Tab. 1.

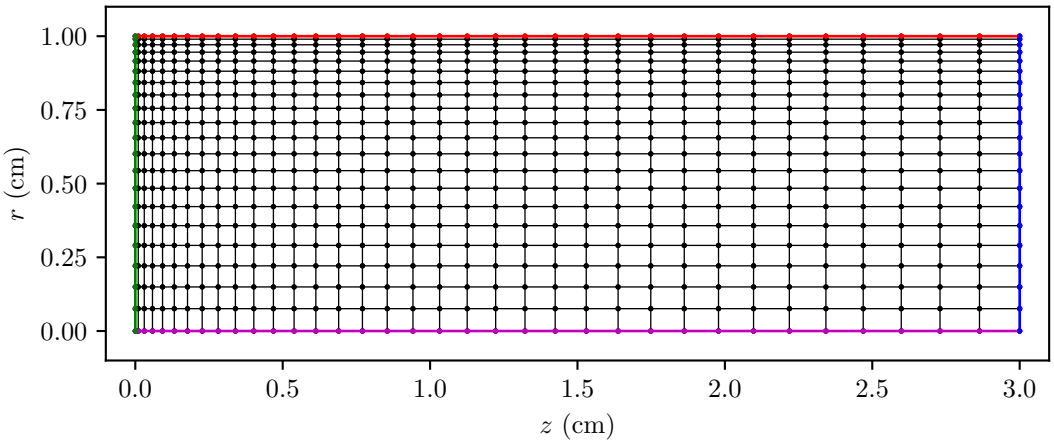

Figure 2: PIC mesh considered in the simulations of neutral reflection effects on the plasma discharge. The red, green, blue and magenta lines indicate the material wall, injection, free loss and symmetry axis at $r = 0$ boundaries, respectively. The radial spacing is minimum close to the walls and the axial spacing is minimum close to the injection surface.

As already mentioned in Sec. 2.1, the reference point for the electric potential where $\phi = 0$, is located at the position $r = z = 0$, while the electron temperature is assumed to be constant everywhere and equal to $T_e = 8$ eV. Neutral xenon atoms are injected with a mass flow $\dot{m}_A = 0.4$ mg/s from a circular injection surface of 1 cm radius at $z = 0$ (green left boundary in Fig. 2) with a flat density profile and sonic conditions $u_n = \sqrt{5T_n/3m_n} = 300$ m/s (for an injection temperature $T_n = 0.073$ eV and an elementary neutral mass $m_n = 2.18 \cdot 10^{-25}$ kg). Collisional effects on heavy species only include single ionization reaction producing Xe^+ ions (no doubly charged ions are considered). Other collisional events, like charge-exchange reactions between ions and neutrals or neutral-neutral elastic collisions, have not been included since preliminary simulations have shown that their effect was clearly negligible (i-n and n-n collisions mean free path is estimated to be 10-50 cm, which is significantly larger than the chamber characteristic size). Ions impacting the chamber lateral material walls (top red boundary in Fig. 2) are neutralized and, as mentioned in Sec. 2.2, recombination neutrals are re-emitted to the simulation domain assuming a wall accommodation coefficient $\alpha_{W,i} = 1$ for the nominal case, with a wall temperature $T_W = 0.0735$ eV (or 850 K), which is equal to the neutral temperature at injection. As already commented in Sec. 2.2, all neutral-wall reflection models consider $\alpha_{W,n} = 0$.

The timestep is set so that, on average, sonic ions take at least two timesteps to cross the smallest cell size in the domain. The simulation duration is 5 ms to ensure stationary conditions are reached for all discharge properties. In order to improve the PIC-related statistics, the heavy species mentioned (neutral and singly-charged ions) are split into three different particle populations, based on their origin. Simulations thus feature injected neutrals, recombination neutrals and ions, with corresponding number densities n_{ni}, n_{nr} and n_i. The numerical discharge ignition is based on a minimum plasma density strategy, as described in the Appendix B, where it is shown to yield the same result as a different approach, relying on initial populations. Finally, all the results presented in the following sections characterizing the steady state discharge are time-averaged over 5000 simulation timesteps (equivalent to 50 μs of simulation time).

The results for the nominal Schamberg neutral-wall reflection case are shown in Fig. 3, in the 2D (z, r) plane of the discharge. Figs. 3(a) and 3(b) show the electric potential and the electric field magnitude (with direction) of the stationary discharge. The axially-averaged radial potential drop from the axis to the dielectric wall sheath edge is $\sim 1.3T_e$. This value is close to the average radial energy gain of the ion population, which features an axially averaged radial fluid Mach number $M_{ri} = u_{ri}/c_s \sim 1.5$ at the sheath edge, with c_s the cold-ion sound

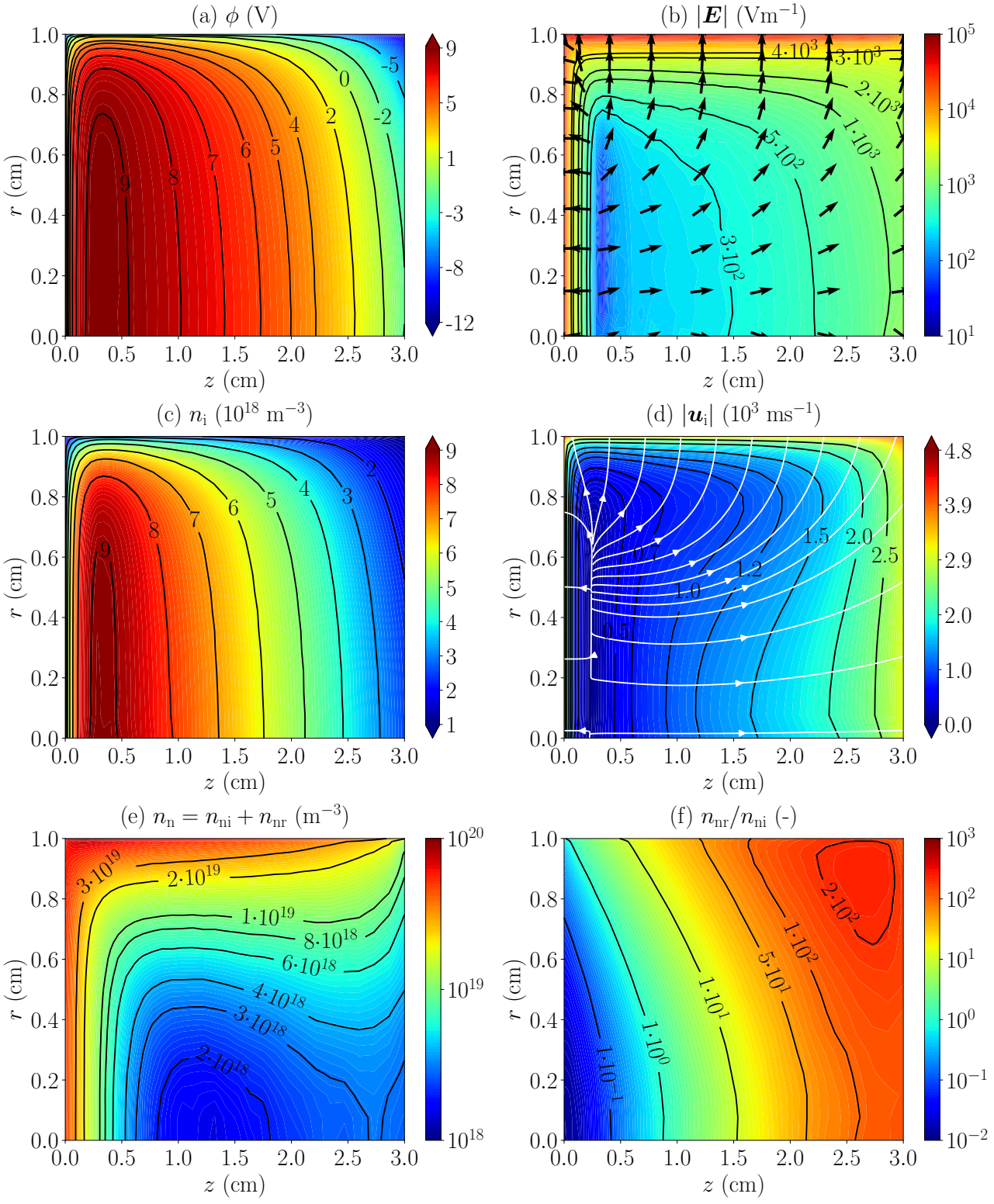

Figure 3: Nominal simulation case results. 2D (z, r) contour maps of (a) electric potential, (b) electric field magnitude and direction, (c) ion (electron) density, (d) ion fluid velocity magnitude and streamlines, (e) total neutral density and (f) ratio between the recombined and the injected neutrals density. In (b) the black arrows indicate the direction of the electric field, while in (d) the white lines represent the ion streamlines. Note that the aspect ratio of the axes is 3:1.

Simulation parameter	Units	Value
Mesh number of nodes, N_r, N_z	-	21, 36
Min. and max axial mesh spacing, Δz	mm	0.1, 1.4
Min. and max. radial mesh spacing, Δr	mm	0.1, 0.8
Simulation timestep, Δt	s	10^{-8}
Simulation duration	ms	5
Injected Xe velocity	m/s	300
Injected Xe temperature	eV	0.0735
Injected Xe mass flow range, $\dot{m}_\mathrm{A}$	mg/s	$0.05 - (0.4)$
Electron temperature, T_e	eV	8
Material wall temperature, T_W	eV	0.0735
Wall accommodation coefficient for neutral reflection $\alpha_{\mathrm{W,n}}$	(-)	0
Wall accommodation coefficient for ion recombination $\alpha_{\mathrm{W,i}}$	(-)	(1),0.99,0.95,0.9
Neutral re-injection model from ion recombination	(-)	D
Neutrals-wall reflection model	(-)	(SC), D, S

Table 1: Main simulation parameters. The nominal case assumptions are indicated in parenthesis: $\dot{m}_\mathrm{A} = 0.4$ mg/s, $\alpha_{W,i} = 1$ and Schamberg neutral reflection model (SC).

speed based on the electron temperature. The electric potential reaches a maximum value of 9.4 V ($\sim 1.2T_e$) at the symmetry axis at $z = 0.28$ cm, and, from this point to the exit section, it drops by 11.4 V ($\sim 1.4T_e$).

Fig. 3(c) depicts the ion density, which, as expected, follows the electric potential distribution, according to Eq. (1). On the other hand, Fig. 3(d) shows the magnitude of the ion fluid velocity and the ion streamlines, which originate at a region featuring a maximum ion production rate at $z \sim 0.25$ cm , thus splitting the domain into regions with positive and negative axial ion flow. The corresponding ion streamlines are consistent with the electric field represented in Fig. 3(b). Finally, Figs. 3(e) and 3(f) plot, respectively, the total neutral density and the recombined-to-injected neutral density ratio $n_\mathrm{nr}/n_\mathrm{ni}$. The injected neutrals only dominate in an initial region at the center of the channel and close to the injection boundary, while the recombined neutrals are responsible for most of the plasma generated downstream of that region (recombined neutral density becomes $\sim$200 times larger than the injected neutral density close to both the downstream boundary and the wall).

3.2 Effects of the neutral-wall reflection physics

In this section, the three different models for the neutral-wall interaction are compared, considering the nominal ion recombination scenario (i.e. $\alpha_{\mathrm{W,i}} = 1$):

- Case SC: Schamberg reflection case with $\nu = 2$ and $\Phi_0 = \pi/2 - \langle\theta\rangle$.
- Case D: purely diffuse reflection case.
- Case S: specular reflection case.

Figs. 4(a) and (b) show the evolution with the neutral injection mass flow $\dot{m}_\mathrm{A}$, at stationary conditions, of the volume-averaged ion and total neutral density, respectively, considering the D, S and SC cases. Figs. 4(c) and 4(d) depict the evolution with the mass flow of the mass utilization and production efficiencies, respectively, defined as

$$\eta_\mathrm{u} = \frac{\dot{m}_{\mathrm{i}\infty}}{\dot{m}_\mathrm{A}}, \qquad \eta_\mathrm{prod} = \frac{I_{\mathrm{i}\infty}}{I_\mathrm{prod}}, \tag{13}$$

where $\dot{m}_{\mathrm{i}\infty} = m_\mathrm{i} I_{\mathrm{i}\infty}/e$ stands for the ion mass flow leaving the domain through the channel exit plane (blue right boundary in Fig. 2), $I_{\mathrm{i}\infty}$ being the corresponding ion current, and I_prod is the total ion current produced. All shown results refer to a steady-state condition after transients have died out.

Fig. 4 shows that, contrary to the D case, in both the SC and S cases, a hysteresis cycle is present, and forward and backward curves have been distinguished with corresponding left-to-right and right-to-left arrows. The forward evolution is obtained by progressively increasing the injected mass flow rate and using a minimum background plasma density of 10^{14} m^{-3} for triggering the discharge (refer to Appendix B). The backward curve results from decreasing the injection mass flow rate, starting from a self-sustained steady plasma discharge.

Focusing first on the forward curves, Fig. 4(a) shows that the minimum injection mass flow for a self-sustained steady plasma discharge depends significantly on the neutral-wall reflection model. A jump in the

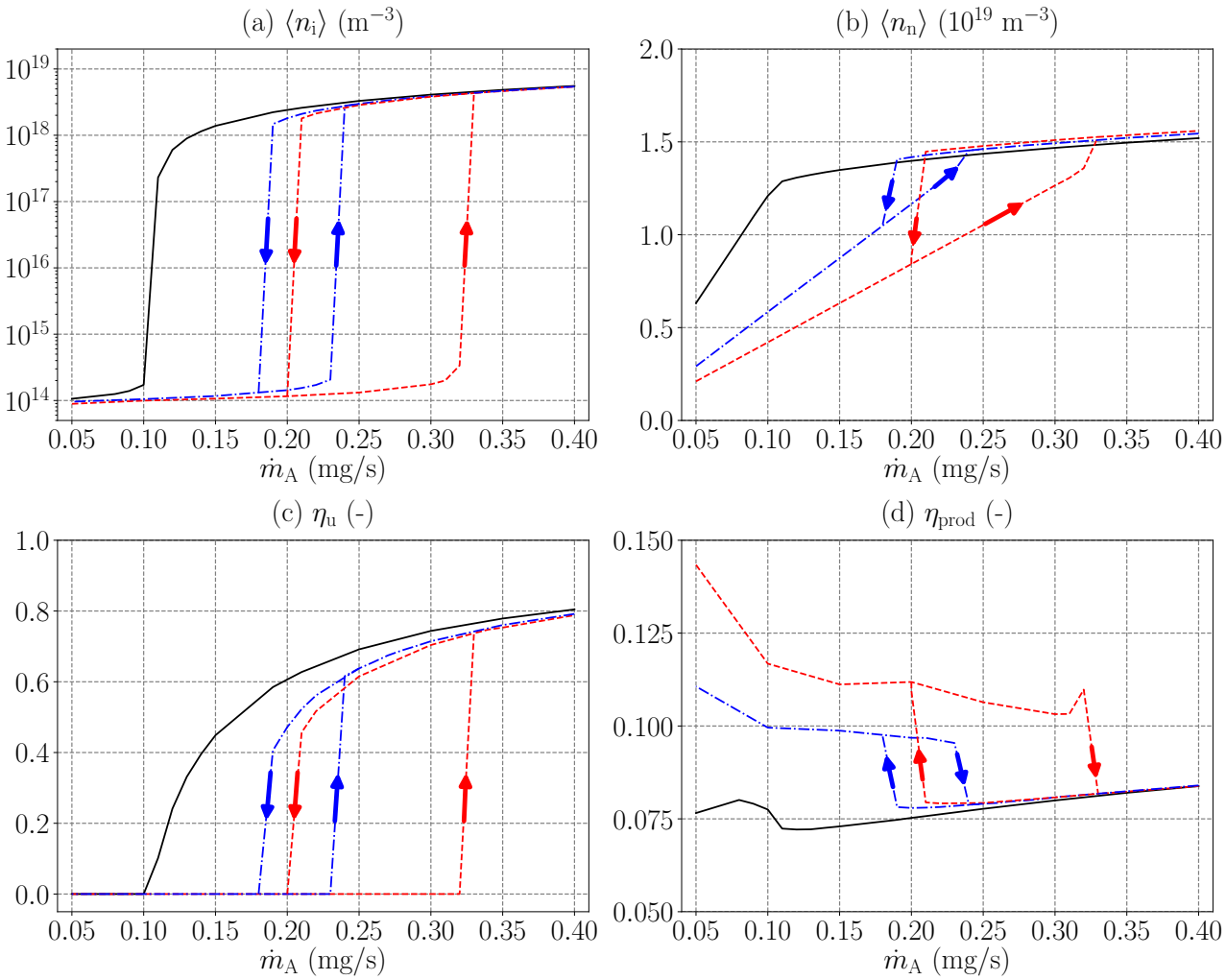

Figure 4: Evolution with the injected mass flow for the D (black solid line), S (red dashed line) and SC (blue dot-dashed line) cases of (a) the volume-averaged plasma density, (b) the volume-averaged total neutral density (including injected and recombination neutrals), (c) the mass utilization efficiency, and (d) the production efficiency. Blue and red left-to-right and right-to-left arrows indicate the forward and backward curves, respectively, for the SC and S cases.

average plasma density in the chamber is found for injection mass flows of ∼0.11, ∼0.24 and ∼0.33 mg/s for the D, SC and S cases, respectively, the former presenting a smoother density evolution with $\dot{m}_\mathrm{A}$. In order to explain the different minimum mass flows, simulations without ionization have been run, in which only injected neutrals are present. Fig. 5 shows the trajectories in the 2D (z, r) half meridian plane of the cylindrical plasma source of three injected neutral macroparticles, which are reflected at the channel lateral wall according to the D (black solid line), S (red dashed line) and SC (blue dot-dashed line) models. The knees in the neutral trajectories in cylindrical coordinates $r(z)$ naturally appear when a macroparticle approaches the axis and reaches its minimum radial distance. The knees occur at the same radial coordinate through the domain for the S case due to the fact that, in a specular reflection with the lateral wall, the reflected particle velocity keeps belonging to the plane formed by the wall normal and the impact velocity (refer to Fig. 1). However, this is not the case for the SC and D cases, in which the trajectory plane can change after every wall impact. Since all reflection processes preserve, on average, the particle energy (i.e. $\alpha_\mathrm{W,n} = 0$), it is evident that the random reflection direction in the D and SC cases considerably increases the neutral residence time in the channel with respect to the S case, as shown in Tab. 2. This implies that, in order to reach the minimum average neutral density to trigger the discharge, which is nearly the same in all cases (see Tab. 2), different mass flows are required.

Fig. 4(b) shows the corresponding average neutral density in the source, which, at the aforementioned minimum mass flow rates, assumes very similar values for all reflection cases ($\langle n_\mathrm{n} \rangle \sim 1.5 \cdot 10^{19} \mathrm{m}^{-3}$). The neutral density increases linearly with the mass flow until a self-sustained plasma discharge is obtained, and then increases with a lower slope, since a higher mass flow yields also a higher ionization efficiency, as shown in Fig. 4(c). While in the D case a smoother η_u evolution is found from $\dot{m}_\mathrm{A} \sim 0.11$ mg/s, in the SC and S cases a more abrupt jump is found, with η_u ∼61% and ∼74% at $\dot{m}_\mathrm{A} \sim 0.24$ and ∼0.33 mg/s, respectively. A maximum

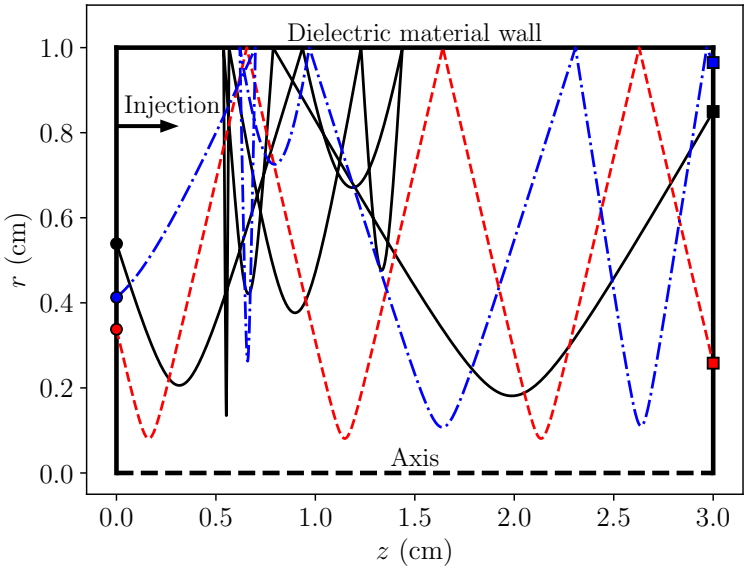

Figure 5: Trajectory of a neutral macroparticle in the 2D (z, r) plane for the D (black solid line), S (red dashed line) and SC (blue dot-dashed line) cases. The circle/square markers identify the neutral initial/final position at the injection/free loss boundary, respectively.

Property	**Units**	**Cases**		
		D	SC	S
$\dot{m}_{\mathrm{A}}$	mg/s	0.11	0.24	0.33
$\langle n_{\mathrm{n}} \rangle$	m^{-3}	$1.28{\cdot}10^{19}$	$1.40{\cdot}10^{19}$	$1.38\ {\cdot}10^{19}$
t_{res}	ms	0.2424	0.1195	0.0859

Table 2: Neutral properties for the D, SC and S cases without ionization at the corresponding minimum $\dot{m}_{\mathrm{A}}$ values yielding a self-sustained steady plasma discharge along the forward curves in Fig. 4. t_{res} is the neutral residence time in the source.

value of ∼80% is obtained in all cases at $\dot{m}_{\mathrm{A}} = 0.4$ mg/s. The production efficiency, on the other hand, presents values ∼8%, meaning that most of the generated ions are lost at the lateral walls of the chamber.

While in the D case no hysteresis is found, in the S and SC cases the results reveal that it is possible to maintain a self-sustained plasma discharge at lower mass flow rates than those corresponding to the forward curve. In particular, in the SC curve, it is possible to reduce the injection mass flow to 0.19 mg/s without extinguishing the discharge. For the S case, the hysteresis cycle is even wider (by a factor of ∼3), and the mass flow can be lowered to 0.21 mg/s. The physical argument behind the onset of a hysteresis cycle relies on the different neutral gas distribution function in the domain before and after a self-sustained steady discharge is achieved. While in the D case the neutral distribution is very similar between these two states, in the S and SC cases, a significant change is induced by the different wall interaction of the reflected and recombination neutrals: the former feature a quasi-specular or specular reflection direction, and the latter are emitted diffusely. This is shown in Fig. 6, which compares the probability distribution of the emission angle θ (refer to Fig. 1) for wall emitted neutrals (including those from both reflection and recombination), $f_{\mathrm{n}}(\theta)$, and the volumetric probability distribution function (averaged over the whole discharge volume) of the neutrals axial velocity, $\tilde{f}_{\mathrm{n}}(v_{\mathrm{z}})$. These results are shown for $\dot{m}_{\mathrm{A}} = 0.21$ mg/s and for all reflection models, with ionization collisions turned either on (black solid lines) or off (red dashed lines). For SC and S cases, the results with ionization collisions activated correspond to the stationary discharges over the backward curves in Fig. 4 at $\dot{m}_{\mathrm{A}} = 0.21$ mg/s. For the D case, Fig. 6(a) show essentially the same $f_{\mathrm{n}}(\theta)$ distribution with and without ionization. Likewise, Fig. 6(d) confirms that the distribution of upstream moving neutrals coincides in the two aforementioned states. On the other hand, for S and SC cases, Figs. 6(b)-(c) show that when a self-sustained steady discharge is achieved (i.e. black solid lines) the average emission angle decreases, indicating more normal wall incidences. Moreover, Figs. 6(e)-(f) reveal a significant increase in upstream moving neutrals (with $v_z < 0$) in the steady discharge (in particular, the S case does not present upstreaming neutrals when ionization is off), which contributes to a higher average neutral residence time in the chamber. The above arguments finally suggest that even the D case could exhibit some kind of hysteresis if a lower ion energy accommodation coefficient $\alpha_{\mathrm{W,i}}$ were considered, which would broaden the neutral energy distribution when a steady self-sustained discharge is achieved.

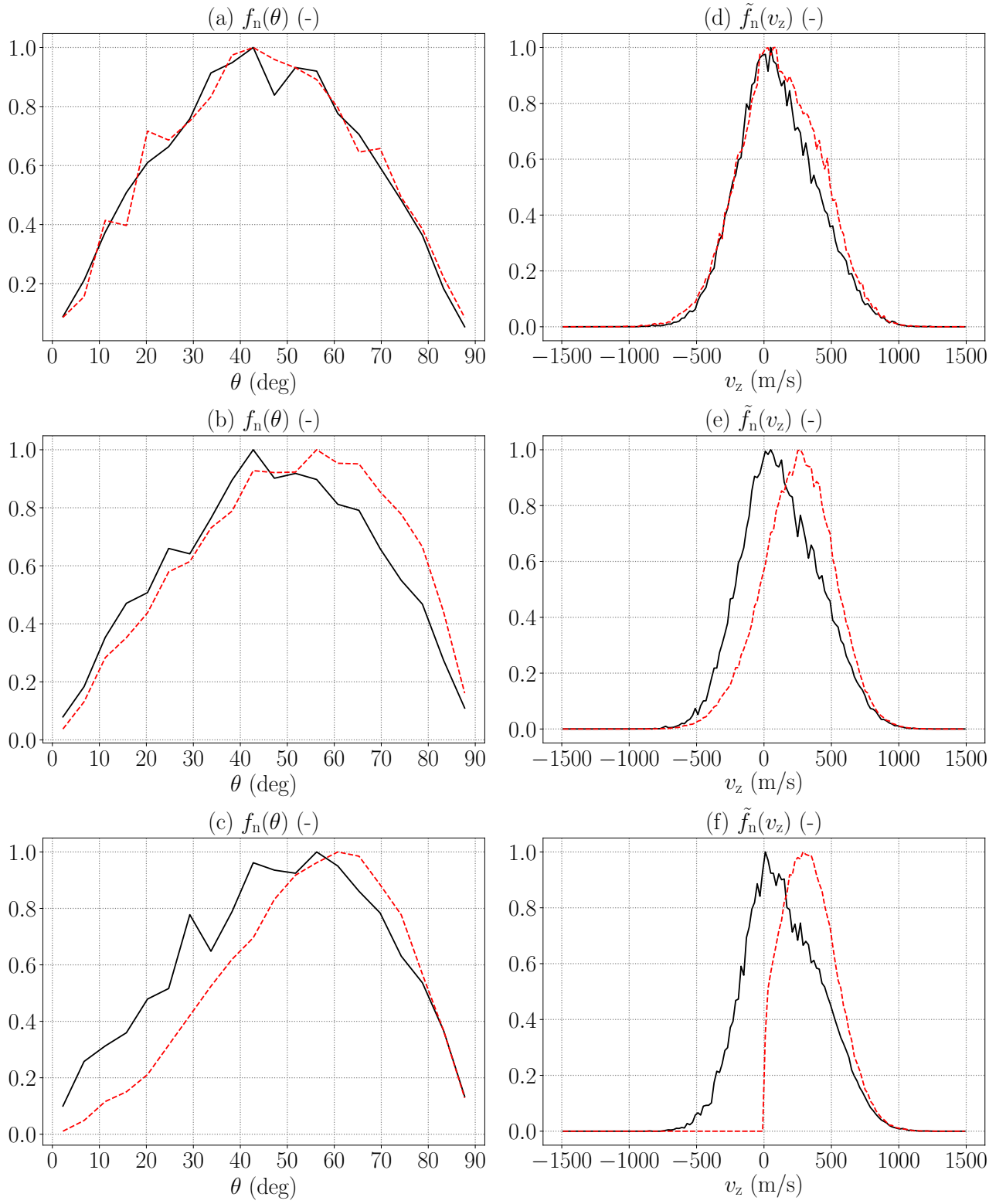

Figure 6: (a)-(c) Probability distribution function of the emission angle θ for wall emitted neutrals, $f_n(\theta)$; and (d)-(f) axial velocity volumetric probability distribution function of discharge neutrals, $\tilde{f}_n(v_z)$, for the D, SC and S cases, respectively, at $\dot{m}_A = 0.21$ mg/s. Black solid and red dashed lines correspond to cases with and without ionization collisions, respectively.

For a self-sustained plasma discharge, the importance of the reflection model on the discharge properties depends strongly on the injection mass flow rate. In particular, Fig. 7 shows a comparison of the axial profiles of ion and neutral density at $\dot{m}_\mathrm{A} = 0.21$ and 0.4 mg/s, for the D, SC and S cases and Tab. 3 lists some relevant parameters of the discharge. While at $\dot{m}_\mathrm{A} = 0.4$ mg/s the plasma profiles and discharge performances are nearly the same, significant changes are observed at $\dot{m}_\mathrm{A} = 0.21$ mg/s, with η_u varying between 45.7% and 62.8% depending on the reflection model. As the injection mass flow is increased, the effect of the neutral wall reflection model become less important due to the dominant ionization. In fact, the ionization mean free path decreases by a factor between 2 and 4 (depending on the model) from $\dot{m}_\mathrm{A} = 0.21$ to 0.4 mg/s. Correspondingly, the utilization efficiency increases and the peak in the plasma density moves upwards. This phenomenon also occurs at $\dot{m}_\mathrm{A} = 0.21$ mg/s due to the stronger influence of the neutral wall-reflection model: the mass utilization increases and the density peak shifts upstream from $z \sim$0.69 to 0.47 cm as the neutral-wall reflection model is changed from a purely specular to a purely diffuse one.

Finally, simulations at different values of the (spatially constant) electron temperature confirm that, in the simplified simulation scenario under consideration, changes in T_e induce similar qualitative changes in the plasma discharge as those observed by varying the mass flow. However, a different behavior could arise if a more complex model for the electron population, including the electron energy equation for updating T_e, were considered.

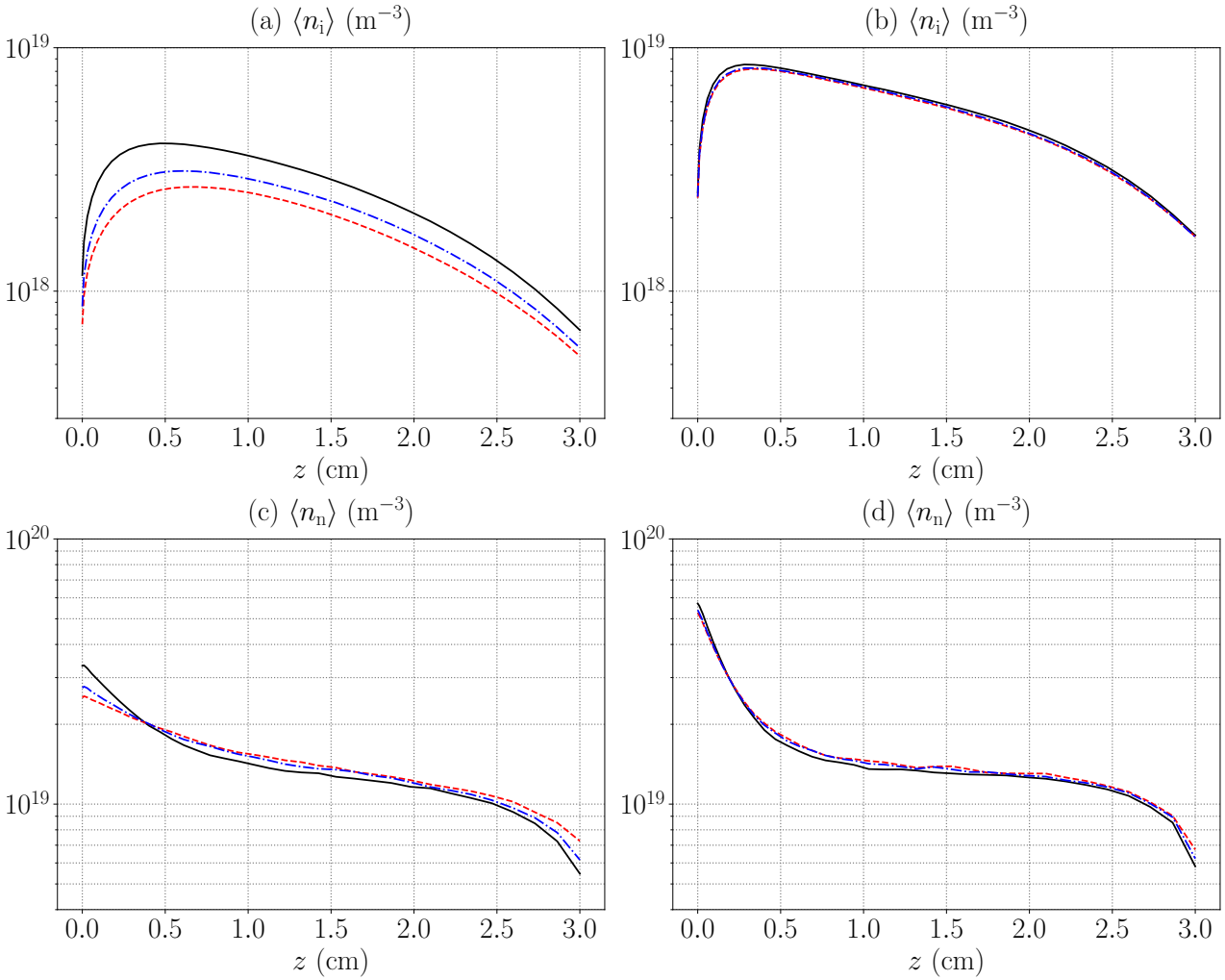

Figure 7: Axial profiles of radially averaged (a)-(b) plasma density and (c)-(d) neutral density. First and second columns correspond to $\dot{m}_\mathrm{A} = 0.21$ and 0.4 mg/s, respectively. Black solid, red dashed and blue dot-dashed lines correspond to D, S and SC cases respectively.

Property	Units	Cases					
		D		SC		S	
$\dot{m}_A$	(mg/s)	**0.21**	**0.4**	**0.21**	**0.4**	**0.21**	**0.4**
η_u	%	62.8	80.5	52.3	79.2	45.7	78.8
η_{prod}	%	7.57	8.38	7.80	8.40	7.94	8.38
$\langle n_n \rangle$	m^{-3}	$1.41 \cdot 10^{19}$	$1.52 \cdot 10^{19}$	$1.43 \cdot 10^{19}$	$1.54 \cdot 10^{19}$	$1.45 \cdot 10^{19}$	$1.56 \cdot 10^{19}$
$\langle n_i \rangle$	m^{-3}	$2.60 \cdot 10^{18}$	$5.54 \cdot 10^{18}$	$2.10 \cdot 10^{18}$	$5.42 \cdot 10^{18}$	$1.79 \cdot 10^{18}$	$5.39 \cdot 10^{18}$
l_{ion}/L	-	$5.61 \cdot 10^{-2}$	$2.48 \cdot 10^{-2}$	$8.81 \cdot 10^{-2}$	$2.76 \cdot 10^{-2}$	$1.14 \cdot 10^{-1}$	$2.82 \cdot 10^{-2}$

Table 3: Relevant discharge properties for D, SC and S cases at $\dot{m}_A = 0.21$ and 0.4 mg/s. The cylindrical channel length is $L = 3$ cm (refer to Sec. 3.1).

3.3 Effects of the ion-wall recombination physics

The effects of the ion-wall recombination physics are discussed in this section. For the nominal neutral reflection case (SC), the simulation results for 4 different accommodation coefficients for the ion recombination $\alpha_{W,i}$ are compared: 1, 0.99, 0.95 and 0.9.

According to Eq. (7), a lower energy accommodation coefficient produces more energetic recombination neutrals (with a higher fraction of the ion impact energy). In all cases analyzed here, the recombination neutrals dominate over the injected ones in most of the chamber (refer to Fig. 3(f) plotting the recombined-to-injected neutral density ratio n_{nr}/n_{ni} for $\alpha_{W,i} = 1$). Since the neutral population is radially confined by the lateral chamber walls and, on the contrary, free to escape axially downwards, the more energetic neutrals present a lower residence time in the chamber and tend to escape downwards more rapidly. As listed in Tab. 4, the resulting lower neutral density in the domain reduces the ionization, yielding a lower plasma density. This fact is confirmed by the ratio between the neutral ionization mean free path and the chamber length l_{ion}/L, which increases by almost one order of magnitude for decreasing $\alpha_{W,i}$ from 1 to 0.9 (see Tab. 4). The lower ionization is responsible for the significant drop in η_u from around 80% down to 20%, while a slighter decrease is found for η_{prod} (refer to values in Tab. 4). Interestingly, the results reveal that the largest relative change (i.e. per unit percentage change in $\alpha_{W,i}$) in the discharge figures of merit occurs for $\alpha_{W,i}$ close to one (i.e. complete thermal accommodation with the walls), thus highlighting the importance of a precise experimental determination of the wall accommodation coefficient for ion recombination, and in particular, its deviation from unity. A similar trend is found in previous studies for a HET discharge [12].

Property	Units	Cases			
		$\alpha_{W,i} = 1$	$\alpha_{W,i} = 0.99$	$\alpha_{W,i} = 0.95$	$\alpha_{W,i} = 0.9$
η_u	%	79.2	57.9	29.7	20.7
η_{prod}	%	8.40	7.12	6.19	6.17
$\langle n_n \rangle$	m^{-3}	$1.54 \cdot 10^{19}$	$1.41 \cdot 10^{19}$	$1.29 \cdot 10^{19}$	$1.26 \cdot 10^{19}$
$\langle n_i \rangle$	m^{-3}	$5.42 \cdot 10^{18}$	$4.69 \cdot 10^{18}$	$2.59 \cdot 10^{18}$	$1.76 \cdot 10^{18}$
l_{ion}/L	-	$2.76 \cdot 10^{-2}$	$4.35 \cdot 10^{-2}$	$1.38 \cdot 10^{-1}$	$2.48 \cdot 10^{-1}$

Table 4: Effects of the recombination coefficient $\alpha_{W,i}$ on relevant discharge properties. The cylindrical channel length is $L = 3$ cm (refer to Sec. 3.1).

In order to analyze the effects of $\alpha_{W,i}$ in the plasma discharge structure, the radially-averaged profiles along z and the axially-averaged profiles along r of the electric potential, plasma density, neutral density, and neutral macroscopic axial velocity are shown in Fig. 8. A decreasing accommodation coefficient $\alpha_{W,i}$ produces a sensibly larger axial potential drop and a smaller potential plateau along the radial direction in a region close to the centerline ($r = 0$), as shown in Figs. 8(a) and 8(b). The plasma density profiles in Figs. 8(c) and 8(d) confirm the aforementioned lower plasma production in the chamber for decreasing $\alpha_{W,i}$. These effects are ultimately related to the neutral dynamics in the chamber as follows. First, focusing on the axial dynamics, the lower neutral residence time in the chamber for decreasing $\alpha_{W,i}$ is consistent with the profiles of the axial component of the neutral macroscopic velocity shown in Figs. 8(g) and 8(h). Mass continuity then imposes a steeper neutral density axial decay, as depicted in Fig. 8(e), and the corresponding lower ion production rate ultimately results in a larger electric potential axial drop according to Eq. (1). Second, the more energetic neutrals for decreasing $\alpha_{W,i}$ tend to fill the chamber more uniformly along the radial direction, as illustrated by the radial neutral

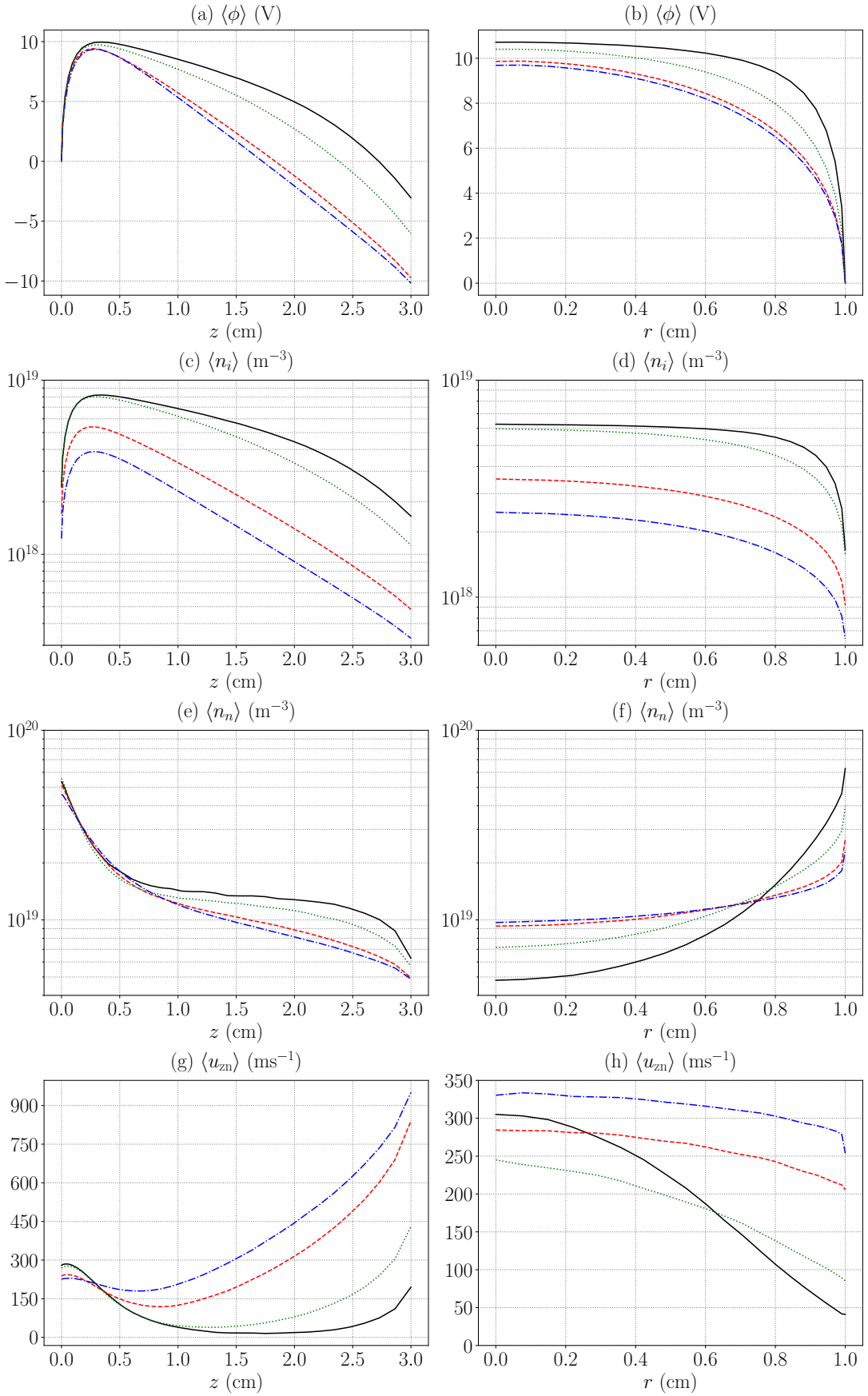

Figure 8: Axial profiles of radially averaged (a) electric potential, (c) plasma density, (e) neutral density and (g) neutral axial macroscopic velocity. Radial profiles of axially averaged (b) electric potential, (d) plasma density, (f) neutral density and (h) neutral axial macroscopic velocity. Black solid, green dotted, red dashed and blue dot-dashed lines correspond to values $\alpha_{\mathrm{W,i}} = 1$, 0.99, 0.95 and 0.9, respectively. The reference for the electric potential is considered at the node with $z = 0$ cm and $r = 1$ cm in (a) and (b), respectively.

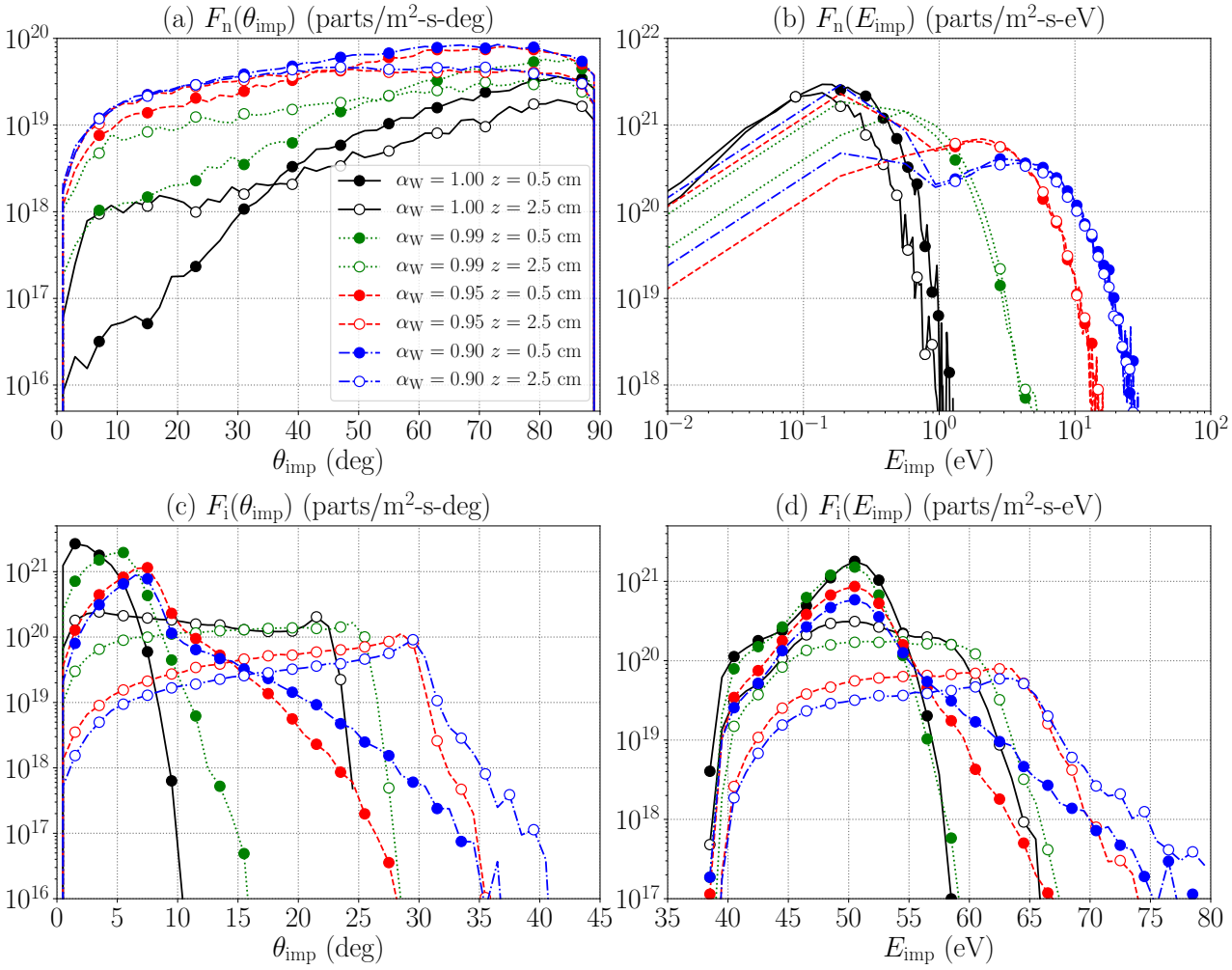

Figure 9: Wall impact angle and impact energy distribution functions for (a)-(b) neutrals and (c)-(d) ions, at $z = 0.5$ cm (filled markers) and $z = 2.5$ cm (empty markers). Black solid, green dotted, red dashed and blue dot-dashed lines correspond to values $\alpha_{W,i} = 1$, 0.99, 0.95 and 0.9, respectively.

density profiles in Fig. 8(f), thus extending the dominant ionization region from the lateral walls and yielding a more uniform plasma production. As a consequence, the electric potential decays radially more uniformly.

Fig. 9 shows the neutral and ion impact angle and impact energy distribution functions at two locations inside the channel $z = 0.5$ cm and $z = 2.5$ cm, for the 4 considered recombination coefficients. Referring to Figs. 9(a) and 9(b) for the neutral population, decreasing $\alpha_{W,i}$ from 1 to 0.9 produces (*i*) a higher contribution of lower impact angles, thus reducing the average impact angle from 70 to 56 deg at $z = 0.5$ cm, and (*ii*) a broadening of the impact energy distribution function, the average impact energy growing from 0.26 eV to 4.88 eV at $z = 0.5$ cm. Moreover, in all cases the average neutral impact angle is quite high (around 60 deg), with a peak of the distribution function at nearly grazing incidences, thus justifying the use of a reflection model that keeps memory of the impact direction, like the Schamberg model.

On the other hand, the impact angle distribution function for the ion population shown in Fig. 9(c) is strongly affected by $\alpha_{W,i}$. In particular, the average impact angle grows along the wall channel, and for decreasing $\alpha_{W,i}$. This is expected because most discharge ions are generated from more energetic recombination neutrals. However, even for the lowest $\alpha_{W,i}$ case at the larger downstream distance, the average impact angle remains quite low (∼20 deg). This nearly normal ion-wall impingement confirms the predominant ion acceleration in the direction perpendicular to the wall occurring inside the plasma sheath and justifies the use of a diffuse re-emission of recombination neutrals from the walls, which keeps no memory of the ion impact direction. The ion energy distribution function shown in Fig. 9(d) reveals two effects on the average impact energy. First it increases downstream along the wall due to the ion axial acceleration [at $z = 2.5$ cm, impact energies are larger due to the axial electric potential drop of Fig. 8(a)]. Second, the low energy tail of the distribution decreases significantly for lower $\alpha_{W,i}$, thus contributing to a higher average impact energy, especially at $z = 2.5$ cm.

To better complement the above results, Fig. 10(a)-(d) shows the axial evolution along the chamber lateral wall of the ion and neutral average impact angle and impact energy for the different values of $\alpha_{W,i}$ considered

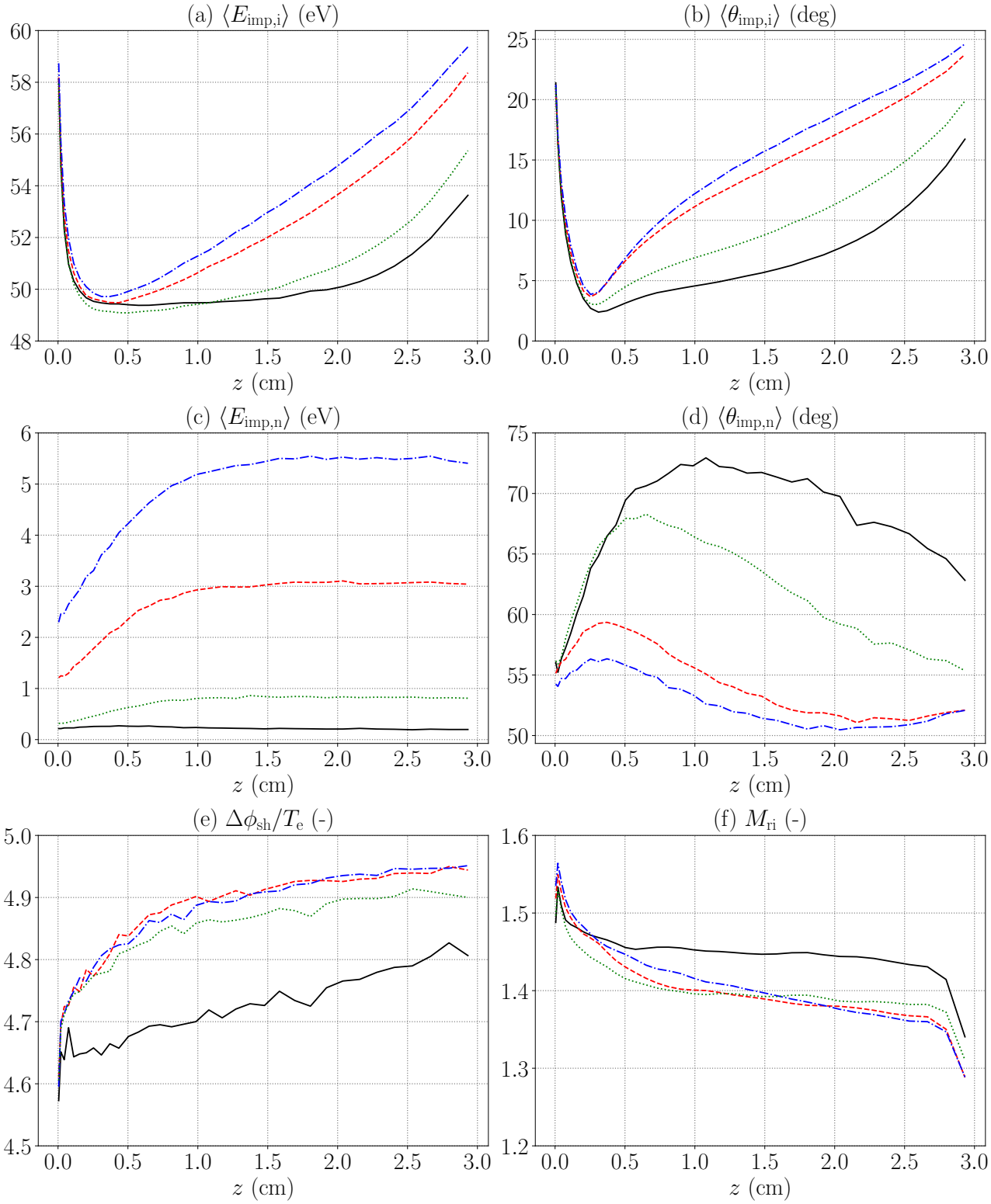

Figure 10: Axial profiles along the dielectric material wall of (a) average ion wall-impact energy, (b) average ion wall-impact angle, (c) average neutral wall-impact energy, (d) average neutral wall-impact angle, (e) sheath potential drop to electron temperature ratio at the wall and (f) normal ion fluid Mach number at the wall. Black solid, green dotted, red dashed and blue dot-dashed lines correspond to cases with $\alpha_{\mathrm{W,i}} = 1$, 0.99, 0.95 and 0.9, respectively.

in this study. These profiles are obtained from the corresponding distribution functions and confirm that the aforementioned trends are independent of the position along the channel lateral wall. In particular, Figs. 10(a) and 10(b) show that, due to the axial ion acceleration, the average ion impact energy and angle grow along the wall upstream and downstream from the region of maximum ion production ($z \sim 0.2$ cm) and, on average, for a decreasing $\alpha_{\mathrm{W,i}}$. On the other hand, Fig. 10(c) confirms the expected monotonic increase of the neutral impact energy with $\alpha_{\mathrm{W,i}}$. Contrary to the ions, the neutral impact angle decreases slightly with z, and, more importantly, it decreases for a decreasing $\alpha_{\mathrm{W,i}}$, as revealed by Fig. 10(d).

The axial profiles of the sheath potential drop $\Delta\phi_{\mathrm{sh}}$ (normalized with the constant electron temperature) and the normal (i.e. radial) ion fluid Mach number at the chamber lateral wall, shown in Figs. 10(e) and 10(f), respectively, are related to those of the ion impact energy and impact angle in Figs. 10(a) and 10(b). According to Eq. (8), the sheath potential drop increases with the axial distance from the injection plane due to the fact that the normal ion fluid Mach number decreases downstream along the wall, as revealed by Fig. 10(f). As commented in Sec. 2, for the present non-monoenergetic ion population, the ion fluid Mach number is higher than the Mach-Bohm in Eq. (9), being the latter larger or equal to 1 to fulfill the kinetic BC.

4 Conclusions

In this work a discharge model for a surface-dominated cylindrical plasma source has been used to analyze the effects of the heavy particles-wall interaction on the discharge. A PIC model is considered for ions and neutrals with an isothermal Boltzmann electrons closure. Regarding the neutral-wall reflection, three models have been presented and compared: purely diffuse and specular reflection models, and the Schamberg reflection model, which retains partially the information of the impact direction. In order to properly compare the three models, neutral-wall interaction has been assumed to be energy-conserving (no energy loss on average). For the ion-wall interaction, on the other hand, a diffuse recombination into neutrals has been considered, with a varying energy wall accommodation coefficient $\alpha_{\mathrm{W,i}}$ between 0.9 and 1.

The neutral gas wall reflection model is shown to play a major role in determining the conditions for a self-sustained and stationary plasma discharge. By varying the neutral gas injection mass flow rate, a hysteresis cycle has been found when neutrals deviate from a purely diffuse reflection at the walls. Forward and backward curves versus the mass flow rate have been identified for the average plasma density and the mass utilization efficiency, among other relevant discharge parameters. Along the forward curves, a jump in the average plasma density in the chamber is found for mass flows of $\sim$0.11, $\sim$0.24 and $\sim$0.33 mg/s for the D, SC and S cases, respectively. This fact has been shown to be induced by the neutral-wall reflection model, which affects significantly the neutral mean residence time and hence the neutral average density in the chamber. For the SC and S cases, the results reveal that, starting from a self-sustained plasma discharge, it is possible to lower the mass flow rate down to 0.19 mg/s and 0.21 mg/s without extinguishing the discharge. It is argued that the hysteresis cycle is due to the abrupt change in the neutral gas distribution function in the chamber before and after a self-sustained steady plasma discharge is achieved. This change is induced by the different wall interaction of the reflected and recombination neutrals: the former feature a quasi-specular or specular reflection in the SC and S models, and the latter are emitted diffusely.

For a self-sustained plasma discharge, the relevance of the reflection model on the discharge properties depends strongly on the injection mass flow rate. Within the mass flow rate range of the hysteresis cycle, the mass utilization efficiency changes up to 20% when neutrals deviate from a purely diffuse reflection, while the plasma density peak in the domain shifts downwards. However, as the gas ionization becomes dominant for higher mass flows, yielding mass utilization values larger than 70%, the neutral-wall reflection effects on the resulting steady plasma discharge become negligible, due to the small ionization mean free path of neutrals compared to the discharge radius. In the simplified isothermal simulation scenario under consideration, the effects of varying the spatially constant electron temperature are qualitatively equivalent to those analyzed for varying the mass flow. However, a different behavior could arise if the electron energy equation were added to the model. This analysis is out of the scope of the present study and is left for future work.

Regarding the ion-wall recombination physics, simulation results show that it strongly affects both the ion and neutral distribution functions, and thus the discharge properties. A lower ion energy accommodation coefficient at the walls produces a more energetic neutral population with a lower residence time, thus yielding a drop in the mass utilization efficiency, which decreases by around 20% for a quite small variation of this coefficient (from 1 to 0.99). This fact reveals the need for a precise experimental estimation of this parameter for accurate simulations. Unfortunately, there is little relevant experimental data on this: the only existing sources refer to very different scenarios, such as the impact of atmosphere neutrals during a re-entry trajectory. Moreover, a decrease in the accommodation coefficient also results in a higher average ion-wall impact energy, and a more grazing ion incidence. Nevertheless, the average ion-wall impact angle remains small (below 20 deg, thus close to wall normal incidence) in all considered cases, which permits to use a simplified recombination

model, featuring a diffuse neutrals re-emission from the walls. It is underlined that this simplification, while being applicable to most plasma sources and thrusters, may not be appropriate at specific chamber locations characterized by a strong ion acceleration parallel to the walls and/or a high secondary electron emission (e.g. at the walls of a HET channel, close to the exit section).

Appendix A: Mesh convergence analysis

The PIC mesh of Fig. 2 has been chosen after a convergence analysis in terms of the radial and axial profiles of certain plasma properties, such as the electric potential or the neutral density. The nominal Schamberg neutral reflection case described in Sec. 3.1 has been considered for the mesh refinement study presented here. The axial (radial) profiles of the radially (axially)-averaged electric potential, ion density and neutral density are compared in Fig. 11(a)-(f) for three different meshes with 11, 16 and 21 nodes along the radial direction and a radial mesh spacing at the first cell at the lateral material wall equal to 0.5, 0.25 and 0.1 mm, respectively, the latter corresponding to the PIC mesh considered for all the results presented in this paper, shown in Fig.2. As it can be observed from the plots (a)-(f), results barely vary when increasing the number of nodes from 16 to 21, so that mesh convergence is achieved with the chosen mesh.

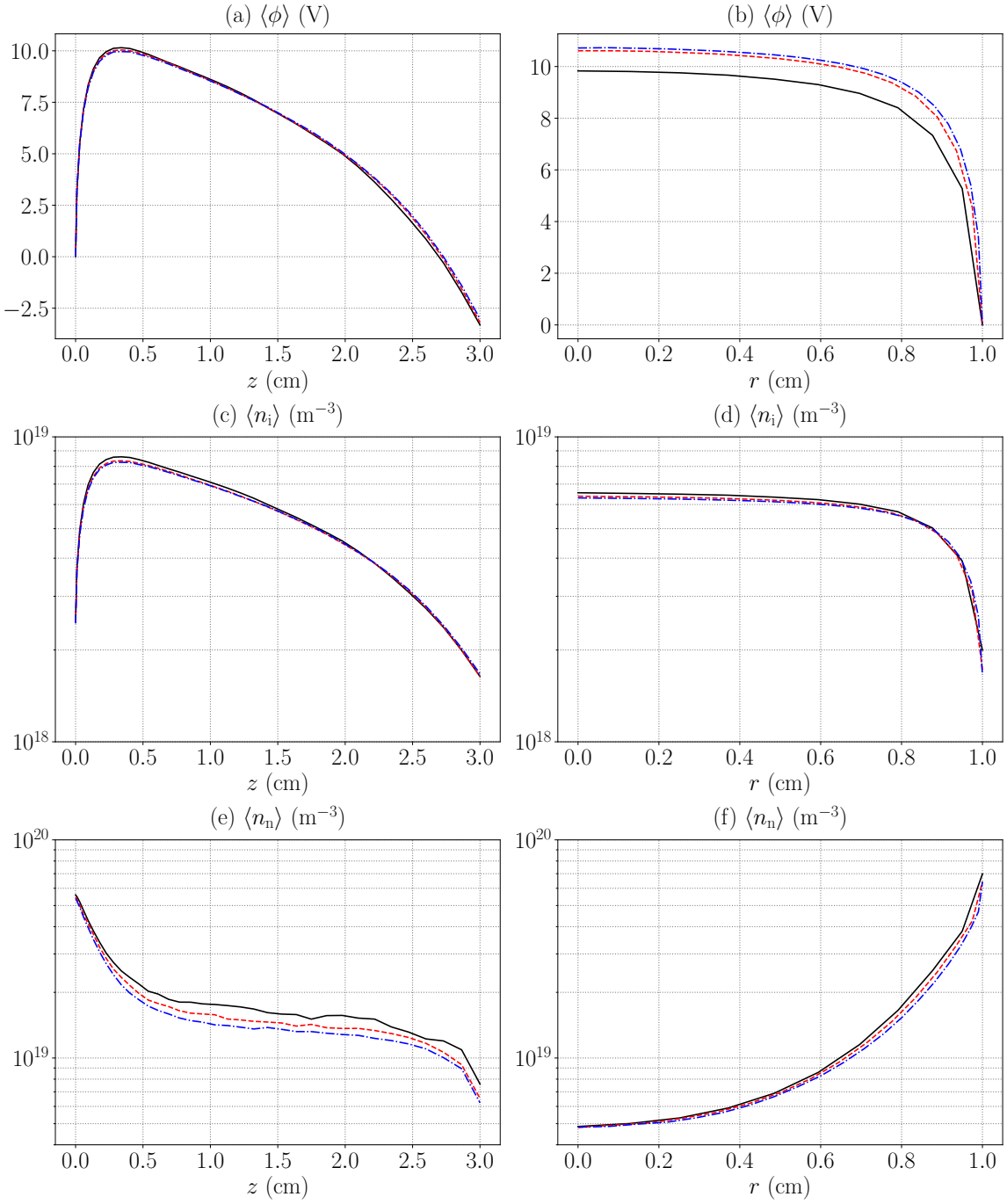

Figure 11: Mesh refinement results comparison for the nominal Schamberg neutral reflection case. Axial profiles of radially-averaged (a) electric potential, (c) ion density and (e) neutral density. Radial profiles of axially-averaged (b) electric potential, (d) ion density and (f) neutral density. Black solid, red dashed and blue dot-dashed lines correspond to simulation domain PIC meshes with 11, 16 and 21 nodes along the radial direction and radial mesh spacing at the dielectric material wall of 0.5, 0.25 and 0.1 mm, respectively

Appendix B: Numerical discharge triggering approaches

Unlike full PIC codes [28], in which also electrons are treated as macroparticles, in the present quasineutral PIC model the electron density equals the ion density. Hence, at the start of the simulation, with only neutrals being injected and present in the simulation domain, it would be impossible to trigger the discharge ignition, unless some numerical artifact is considered. This may consist in either considering a minimum background ion density for ionization or, partially equivalently, a given initial ion population, which is permitted to evolve in time. Both approaches are analyzed and compared here in terms of stationary discharge solutions and computational cost of the quasineutral ignition transient. In the minimum background density approach (MD), a minimum plasma density is considered for the ionization reactions only if the weighted plasma density (from the ion macroparticles) is locally lower. In order not to affect the discharge, this minimum plasma density should be low enough, in this case set to 10^{14} m^{-3}, and once the plasma density in the chamber is everywhere larger than this, it will no longer affect the simulation.

In the initial ion population approach (IP), a population of ions is uniformly distributed in the simulation domain. If a self-sustained plasma discharge is finally achieved, as the simulation advances, this initial ion population is gradually lost due to either recombination with the walls or crossing of the external simulation boundaries. For this comparison study, an initial ion population of 50 macroparticles per cell yielding a uniform plasma density of 10^{17} m^{-3} is distributed in the simulation domain.

For the nominal case of Sec. 3.1, Figs. 12(a) and 12(b) compare the time evolution of the average ion and neutral particle density in the simulation domain obtained when applying the two approaches (MD and IP). Interestingly, both approaches present a similar transient, especially for the neutral population, and, as expected, the same steady state discharge properties. It is worth to notice that the total computational time in the IP case is around 10% higher than that of the approach MD, so that the latter ignition strategy has been considered for the simulations shown in this paper.

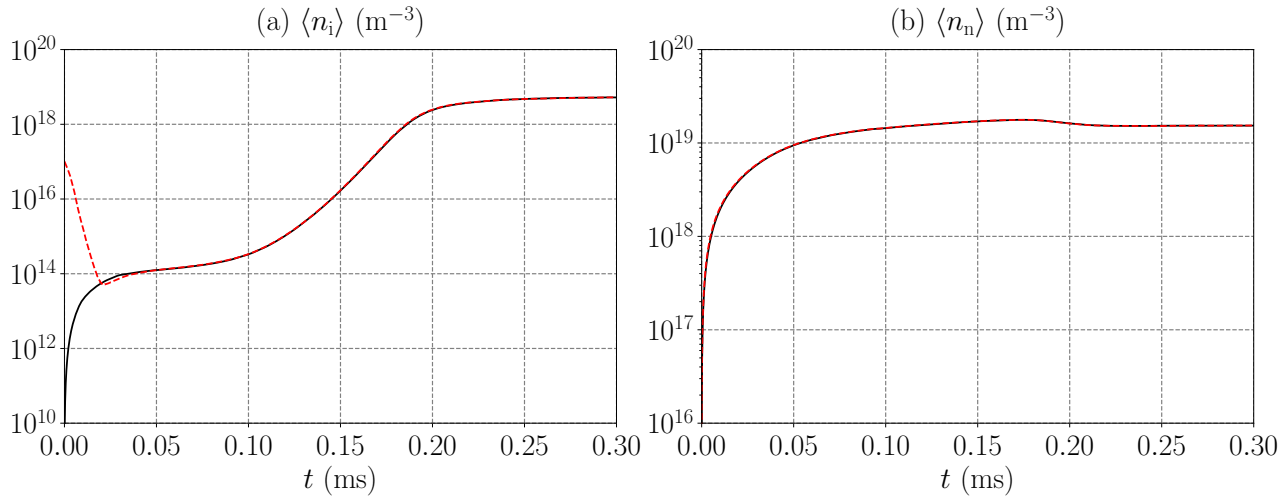

Figure 12: Time evolution of (a) the average ion density and (b) the average neutral density in the simulation domain. Black solid and red dashed lines corresponds to MD and IP approaches, respectively.

Acknowledgments

This paper has been funded mainly by Comunidad de Madrid/FEDER/FSE, through the PROMETEO-CM project, Grant number Y2018/NMT-4750. Additional support came from the ESPEOS project, funded by the Agencia Estatal de Investigación (Spain's National Research and Development Plan), under Grant number PID2019-108034RB-I00/AEI/10.13039/501100011033.

References

[1] Ahedo, E., "Plasmas for space propulsion," *Plasma Physics and Controlled Fusion*, Vol. 53, No. 12, 2011, pp. 124037.

[2] Taccogna, F. and Garrigues, L., "Latest progress in Hall thrusters plasma modelling," *Reviews of Modern Plasma Physics*, Vol. 3, No. 1, 2019, pp. 12.

[3] Boeuf, J., "Tutorial: Physics and modeling of Hall thrusters," *J. Applied Physics*, Vol. 121, No. 1, 2017, pp. 011101.

[4] Gibson, A. R., Foucher, M., Marinov, D., Chabert, P., Gans, T., Kushner, M. J., and Booth, J.-P., "The role of thermal energy accommodation and atomic recombination probabilities in low pressure oxygen plasmas," *Plasma physics and controlled fusion*, Vol. 59, No. 2, 2017, pp. 024004.

[5] Domínguez-Vázquez, A., Zhou, J., Fajardo, P., and Ahedo, E., "Analysis of the plasma discharge in a Hall thruster via a hybrid 2D code," 36^{th} *International Electric Propulsion Conference*, No. IEPC-2019-579, Electric Rocket Propulsion Society, Vienna, Austria, 2019.

[6] Ortega, A. L., Mikellides, I. G., and Chaplin, V. H., "Numerical Simulations for the Assessment of Erosion in the 12.5-kW Hall Effect Rocket with Magnetic Shielding (HERMeS)," *35th International Electric Propulsion Conference, Atlanta, GA, IEPC-2017-154*, 2017.

[7] Bird, G., *Molecular Gas Dynamics and the Direct Simulation of Gas Flows*, The Oxford Engineering Science Series, Oxford University Press, Oxford, UK, 1994.

[8] Moe, K. and Moe, M., "Gas–surface interactions and satellite drag coefficients," *Planetary and Space Science*, Vol. 53, No. 8, 2005, pp. 793–801.

[9] Prieto, D. M., Graziano, B. P., and Roberts, P., "Spacecraft drag modelling," *Progress in Aerospace Sciences*, Vol. 64, 2014, pp. 56–65.

[10] Gregory, J. and Peters, P., "A measurement of the angular distribution of 5 eV atomic oxygen scattered off a solid surface in earth orbit," *15th International Symposium on Rarefied Gas Dynamics*, Vol. 2, 1987, pp. 644–654.

[11] Chirita, V., Pailthorpe, B., and Collins, R., "Gas-surface interactions in the thermal and sub-thermal regime: a molecular dynamics study," *Nuclear Instruments and Methods in Physics Research Section B: Beam Interactions with Materials and Atoms*, Vol. 124, No. 1, 1997, pp. 12–22.

[12] Ahedo, E., Gallardo, J., and Martínez-Sánchez, M., "Effects of the radial-plasma wall interaction on the axial Hall thruster discharge," *Physics of Plasmas*, Vol. 10, No. 8, 2003, pp. 3397–3409.

[13] Font, G. I., "Computational acceleration of orbital neutral sensor ionizer simulation through phenomena separation," *Journal of Computational Physics*, Vol. 316, 2016, pp. 1–9.

[14] Rehker, S. and Wobig, H., "A kinetic model for the neutral gas between plasma and wall," *Plasma Physics*, Vol. 15, No. 11, 1973, pp. 1083.

[15] Hackmann, J., Kim, Y., Souw, E., and Uhlenbusch, J., "Investigation of neutral particle behaviour between plasma and wall including wall interactions," *Plasma Physics*, Vol. 20, No. 4, 1978, pp. 309.

[16] Domínguez-Vázquez, A., Cichocki, F., Merino, M., Fajardo, P., and Ahedo, E., "Axisymmetric plasma plume characterization with 2D and 3D particle codes," *Plasma Sources Science and Technology*, Vol. 27, No. 10, 2018, pp. 104009.

[17] Saltsburg, H., Smith, Jr., J. N., and Rogers, M., *Fundamentals of gas-surface interactions*, Academic Press, New York and London, 1967.

[18] Thomas, L., "Accommodation of molecules on controlled surfaces- Experimental developments at the University of Missouri, 1940-1980," *12th International Symposium on Rarefied Gas Dynamics*, paper 217, pp. 83–108, American Institute of Aeronautics and Astronautics, https://www.aiaa.org, Charlottesville, VA, USA, July 7-11, 1980.

[19] Anton, A. and Ahedo, E., "Contour algorithms for a Hall thruster hybrid code," *42nd Joint Propulsion Conference*, AIAA-2006-4834, American Institute of Aeronautics and Astronautics, Sacramento, CA, USA, July 9-12, 2006.

[20] Ahedo, E., Antón, A., Garmendia, I., Caro, I., and Amo, J. d., "Simulation of wall erosion in Hall thrusters," *30th International Electric Propulsion Conference, Florence, Italy*, IEPC 2007-067, 2007.

[21] Liu, L., Cai, G., Zheng, H., Shang, S., and He, B., "Measurement of the momentum accommodation coefficient for the interactions between electric thruster plume and a solid surface," *Physics of Plasmas*, Vol. 27, No. 5, 2020, pp. 053511.

[22] Cichocki, F., Domínguez-Vázquez, A., Merino, M., and Ahedo, E., "Hybrid 3D model for the interaction of plasma thruster plumes with nearby objects," *Plasma Sources Science and Technology*, Vol. 26, No. 12, 2017, pp. 125008.

[23] Fife, J., *Hybrid-PIC Modeling and Electrostatic Probe Survey of Hall Thrusters*, Ph.D. thesis, Massachusetts Institute of Technology, 1998.

[24] Mitchner, M. and Kruger Jr., C., *Partially ionized gases*, John Wiley and Sons, Hoboken, NJ, 1973.

[25] Moore, P. and Sowter, A., "Application of a satellite aerodynamics model based on normal and tangential momentum accommodation coefficients," *Planetary and space science*, Vol. 39, No. 10, 1991, pp. 1405–1419.

[26] Harrison, E. and Thompson, W., "The low pressure plane symmetric discharge," *Proceedings of the Physical Society*, Vol. 74, No. 2, 1959, pp. 145.

[27] Ahedo, E., Santos, R., and Parra, F., "Fulfillment of the kinetic Bohm criterion in a quasineutral particle-in-cell model," *Physics of Plasmas*, Vol. 17, No. 7, 2010, pp. 073507.

[28] Taccogna, F., Schneider, R., Longo, S., and Capitelli, M., "Kinetic simulations of a plasma thruster," *Plasma Sources Science and Technology*, Vol. 17, No. 2, 2008, pp. 024003.